Azimuthal Fourier decomposition for loss analysis of hollow-core tube lattice fibers part I: Ideal fibers

Federico Melli [a], Kostiantyn Vasko [b], Lorenzo Rosa [a], Fetah Benabid [b], Luca Vincetti [a,*]

[a] *Department of Engineering "Enzo Ferrari", University of Modena and Reggio Emilia, via Vivarelli 10, Int. 1, Modena, 41125, Italy*
[b] *GPPMM Group, XLIM Institute, UMR CNRS 7252, University of Limoges, Limoges, France*

A B S T R A C T

This is the first part of two papers where we propose and apply a methodology for confinement loss analysis in tube lattice fibers (TLFs). The methodology is based on azimuthal Fourier decomposition (AFD) of the fiber's cladding and core modes along the perimeters of the cladding tubes composing. This technique, combined with coupled mode theory, constitutes an effective approach to gain insight in the inhibited coupling waveguiding mechanism and design, along with fiber non-idealities impact on confinement loss. In this part I, we describe the approach and apply it to loss analysis of ideal TLFs. The approach is then applied to the analysis of the effects of tube thickness variation in part II.

1. Introduction

Modern optical systems require light guidance media that combine highly sought features such as very low loss, high power-handling capabilities, and strong interaction with gases and liquids. Hollow-core photonic-crystal fibers (HC-PCFs) are highly investigated in this regard, as they offer the ability to satisfy all these requirements at the same time, owing to their ability to guide light in a hollow core where it has minimal interaction with the dielectric cladding, making them attractive in applications as diverse as gas lasers (Debord et al., 2015; Nampoothiri et al., 2012), light-gas interaction (Debord et al., 2019; Hoang et al., 2020), terahertz systems (Setti et al., 2013), gas- and bio-sensing (Jaworski et al., 2020; Bomse and Ediger, 2014; Khozeymeh et al., 2022), and classical (Hong et al., 2021) and quantum communications (Chen et al., 2021).

Their guidance mechanism relies on preventing the core-guided mode from coupling to the cladding by either photonic bandgap (PBG) (Cregan et al., 1999) or inhibited coupling (IC) guidance (Couny et al., 2007). In IC fibers, core and cladding modes (CMs and CLMs respectively) with the same effective index are prevented from coupling by increasing the CLMs field transverse oscillation frequency, and by minimizing their transverse field spatial-overlap with that of the core modes (Couny et al., 2007; Vincetti and Setti, 2010; Debord et al., 2017). An effective way to strengthen these effects is to deploy hypocycloid core-contour (i.e. negative curvature) fiber designs (Wang et al., 2011), which dramatically reduce transmission loss and optical overlap with the dielectric material of the cladding (Debord et al., 2013a). Whilst the principles of IC guidance and the criteria for decreasing

the IC fibers' transmission loss are known and exemplified by the introduction of the negative curvature core contour (Debord et al., 2019), there is thus far no in-depth treatment for CMs-CLMs coupling. This, in turn, strongly limits the prediction power in designing IC fibers and the explanation of their defining properties such as scaling of CL with wavelength, transmission band width, polarization dependence of the coupling between core and cladding modes. This situation primarily results from the fact that the analysis of HCPCF guidance has predominantly relied on numerical simulation tools, with limited utilization of analytical or semi-analytical approaches.

From this regard, single ring hollow core Tube Lattice Fibers (TLFs) provide an excellent platform to investigate the coupling between CMs and CLMs in Inhibited-Coupling Hollow-Core Photonic Crystal Fibers (IC-HCPCF). TLFs achieve a negative curvature core by utilizing a cladding structure consisting of thin isolated dielectric tubes arranged around the hollow core (Vincetti and Setti, 2010; Pryamikov et al., 2011). These fibers have demonstrated impressive reductions in transmission loss (Debord et al., 2017; Pryamikov et al., 2011; Belardi and Knight, 2014; Jasion et al., 2022; Gao et al., 2019; Amrani et al., 2021; Osório et al., 2023), and possess desirable properties such as wide transmission bandwidth, low loss, low dispersion, and a relatively simple cladding structure (Debord et al., 2017). The simplicity of the cladding structure in TLFs, combined with the mathematical expressions for the dielectric modes of a single tube (Kharadly and Lewis, 1969) makes them an ideal platform for developing mathematical models to analyze IC guidance. Such models can help explain the discrepancy between experimentally measured loss and the theoretically

---

achievable minimum confinement loss (CL) in real fibers (Debord et al., 2017; Ding et al., 2020). Real fibers exhibit non-ideal structures with imperfections like glass surface roughness caused by frozen-in thermal surface capillary waves (SCW) during fiber drawing (Roberts et al., 2005), deformations of the fiber cross section (Weiblen et al., 2016), and micro-bending loss (Sakr et al., 2020). However, there is currently a lack of comprehensive theoretical analysis thoroughly examining the impact of these geometric imperfections on the CL of HCPCFs.

The objective of this series of papers (Part I, the current paper, and the subsequent Part II Melli et al., 2022) is to address, to some extent, the existing knowledge gap. In this paper, we introduce and establish an analysis technique utilizing the Azimuthal Fourier Decomposition (AFD) of the fiber's modes. This method, when employed on ideal TLFs, demonstrates a promising capability to model the interactions between Core Modes (CMs) and Cladding Modes (CLMs), and determine their influence on CL. In the subsequent paper (Melli et al., 2022), we will further explore and expand upon these findings to analyze the effect of tube thickness variation on TLF modal spectrum and transmission spectral structure and loss.

2. Inhibited-coupling waveguiding

Here, we briefly recap the fundamental principles of the Inhibited Coupling model. HCPCFs can be considered as comprised of two distinct regions with different sets of modes: the core and the surrounding cladding. Core modes, mainly confined in the fiber hollow core, exhibit low transmission loss only if they are strongly decoupled from the highly lossy cladding modes. In other words, it is crucial to minimize or ideally eliminate the transfer of power from the core modes to the cladding modes. According to Coupled Mode Theory (CMT), the optical power transfer from core modes to cladding modes occurs when both longitudinal and transverse phase matching conditions are satisfied. This implies the simultaneous fulfillment of the following criteria (Kogelnik, 1988):

- longitudinal phase matching $n_{eff_{co}} = n_{eff_{cl}}$;
- non-zero overlap integral $K = \iint_{S_\infty} \overline{E}_{t_{co}} \cdot \overline{E}_{t_{cl}} \, dS \neq 0$.

Here, $n_{eff_{co}}$ and $n_{eff_{cl}}$ are the effective indices and $\overline{E}_{t_{co}}$, and $\overline{E}_{t_{cl}}$ are the transverse components of the electric field of the CM and CLM, respectively. Alternatively, we can state that in order to achieve low loss in HCPCFs, it is sufficient for at least one of the two aforementioned conditions to not be satisfied.

In Photonic Band-Gap HCPCFs (PBG-HCPCFs), the first condition is inherently unfulfilled since there are no Cladding Modes (CLMs) that have the same effective index as the core mode. This absence of CLMs at the core effective index naturally results in a complete elimination of the overlap integral. In contrast, in IC-HCPCFs, the first condition cannot be avoided due to the existence of a quasi-continuum of CLMs that are longitudinally phase-matched with CMs (Debord et al., 2019). However, despite this, IC-HCPCs can exhibit extremely low CL. This stems from the overlap integral K reaching close-to-zero values when CLMs exhibit quick spatial oscillations (more accurately, quick spatial oscillations along the tubes' perimeters; see Supplementary Material in Debord et al. (2017)) and strong light confinement within the tubes' dielectric material. Consequently, in IC-HCFs the CL and its spectrum are chiefly driven by the CLMs field spatial structure at their crossing point with CMs in effective index-frequency space. We note that the CMs and CLMS strong coupling inhibition is akin to bound state in a continuum (BIC) when the integral K is nil, and to quasi-BIC when K is close-to-zero (Couny et al., 2007; Hsu et al., 2016).

In order to analyze this CMs-CLMs coupling, we proceed with the following approximations. First, we only consider Fundamental Core Mode (FCM) (i.e. the LP_{01}-like mode), and set its effective index to 1, i.e. the $n_{eff_{co}} = 1$. This approximation is justified by the fact that, in IC-HCPCFs, FCM effective index is very close to unity, with a relatively
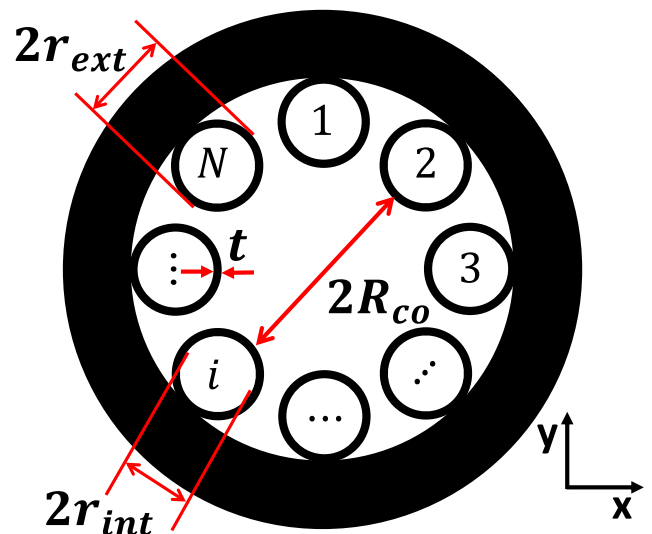

Fig. 1. Cross-section of an 8-tube TLF.

weak variation versus frequency over its transmission bandwidth and it allows to estimate the frequency corresponding to the longitudinal phase matching condition with the CLM cut-off frequency. Second, in Tube Lattice Fibers (TLFs), shown in Fig. 1, the larger distance between adjacent tubes compared to the glass tube-thickness and working wavelength puts us in the regime of large pitch (Debord et al., 2019). This enables a simplified analysis of Cladding Modes (CLMs) using the single-tube approximation, where each CLM can be considered as a combination of modes from the individual tubes with identical transverse effective index and field profile:

$$\overline{E}_{t_{cl}} = \sum_{i=1}^{N} \overline{E}_{t_{cl_i}}. \tag{1}$$

Hence, the field distribution and dispersion curve are well approximated by those of an isolated single tube completely surrounded by air (Vincetti and Rosa, 2019). Hereafter we will refer to the modes confined within the dielectric of a single isolated tube as CLMs. Thanks to that, the integral to calculate K can be split into the sum of N terms, one for each tube composing the cladding:

$$K = \sum_{i=1}^{N} K_i = \sum_{i=1}^{N} \iint_{S_{tube_i}} \overline{E}_{t_{co}} \cdot \overline{E}_{t_{cl_i}} \, dS, \tag{2}$$

where now $\overline{E}_{t_{cl_i}}$ is the CLM electric field transverse component of the ith tube composing the cladding and S_i is a domain containing and surrounding the tube defined so that $\overline{E}_{t_{cl_i}}$ is negligible outside of it (see Supplementary Material in Debord et al. (2017)). CLMs can be classified into $HE_{\mu,\nu}$ and $EH_{\mu,\nu}$ modes where μ and ν are the mode field azimuthal and radial indices, respectively (Kharadly and Lewis, 1969). The two mode families differ in their field polarization. The $EH_{\mu,\nu}$ modes have predominantly radial polarization, while the $HE_{\mu,\nu}$ modes have predominantly azimuthal polarization. A detailed description of the single tube modal properties can be found in Vincetti and Setti (2010), Debord et al. (2017), and Vincetti and Rosa (2019).

Since the azimuthal index μ determines the CLM electric field spatial oscillation along the tube perimeter, the magnitude of K, and thus the CL spectrum, are directly related to μ and to how the CLMs cut-off frequencies change in relation to it.

Fig. 2 illustrates this point for TLF Fiber #1 (see Table 1 and Fig. 1 for the fiber geometrical parameters). $F = \frac{2t}{\lambda}\sqrt{n_d^2 - 1}$ is the normalized frequency being n_d the tube refractive index and λ the wavelength. Fig. 2(a) shows the $\mu - F$ curves, which show the link between the CLM
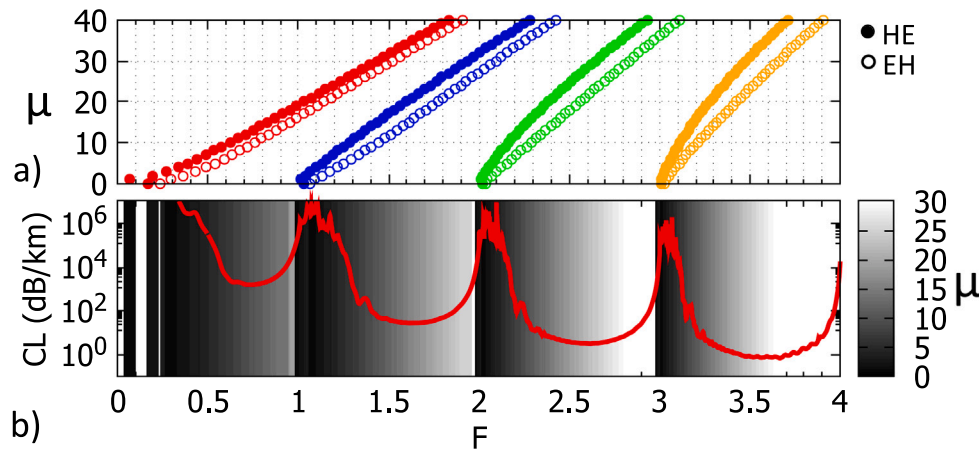
Fig. 2. Fiber #1. (a): cut-off frequencies F_c of CLMs HE (filled circles) and EH (empty circles) by varying the azimuthal index μ and for four values of the radial index ν ($\nu = 1$ red; $\nu = 2$ blue; $\nu = 3$ green; $\nu = 4$ orange). (b): CL of the LP_{01} FM. Background color related to the azimuthal index of the CLM having cut-off frequency F. (For interpretation of the references to color in this figure legend, the reader is referred to the web version of this article.)

cut-off frequency $F_c^{\mu,\nu}$ and its indices μ and ν both for HE and EH CLMs. Four distinct branches of positively sloped curves are observed, each associated with a constant radial index ν. Notably, HE modes exhibit steeper slopes and slightly lower cut-off frequencies compared to EH modes. The red curve in Fig. 2(b) shows the CL loss spectrum with its spectral structure consisting of low loss transmission bands (TB) and high loss region (HLR) edges located at $F = \nu - 1$. In this context, the radial index ν represents the TB order.

By comparing the spectral evolution of CMs with CL spectrum structure of the FCM, several important observations can be made. It is evident that the fiber TB red-edge corresponds to cut-off frequencies of the $HE_{0,\nu}$ CLMs, i.e. $F_c = \nu - 1$. These frequencies align with values commonly used in anti-resonant reflecting optical waveguide (ARROW) literature (Debord et al., 2019; Duguay et al., 1986). However, the ARROW model disregards the presence of CLMs and their coupling with CMs. Fig. 2(b) clearly shows that the HLRs structure and frequency location are more intricate to be solely attributed to resonances at $F = \nu - 1$. The shape of the HLRs and the observed correlation between CL decrease with the μ slope at their blue-edges are some of the examples that emphasize the limitations of the ARROW model in comprehensively explaining the behavior of CLMs and their influence on the overall CL spectrum. To better illustrate the correlation between the FCM CL decrease and cladding mode azimuthal index μ increase, the background of Fig. 2(b) is gray-scaled according to the lowest value of the azimuthal index μ of the CLM (i.e. that of $EH_{\mu,\nu}$). The darker color corresponds to the smaller values of μ, and the lighter color to the larger values. We clearly note that the HLRs correspond to the darkest regions, which is consistent with our expectation of a larger coupling coefficient K between CMs and low azimuthal index CLMs (Couny et al., 2007; Debord et al., 2013b). By increasing the frequency, the azimuthal index increases, which in turn induces a reduction in the coupling factor K and thus in CL (Debord et al., 2017). The decrease in confinement loss continues until the normalized frequency approaches the next integer value, i.e. $F = \nu$, where CL once again starts to increase. This increase appears with the end of the first-order TB and the onset of the modes $EH/HE_{0,\nu+1}$ associated with the second branch in the $\mu - F$ curves (Fig. 2(Top)). This correlation between CL and CLMs is replicated for every TB, with the difference, however, that as the TB order (i.e. the CLMs radial index ν) increases, the bandwidth of the HLR narrows down, and the TB minimum CL further decreases. The spectral narrowing of HLR is explained with the steeper slope of the μ-curves for larger radial index value (see Fig. 2(Top)). It is worth noting that the HLRs are characterized by the presence of CLMs with lower values of azimuthal index μ, typically around 10 or lower.

Table 1
TLF parameters. All geometrical parameters are given in microns.

Fiber	t	r_{ext}	n_d	N	R_{co}	ρ
#1	0.75	6.0	1.45	8	13.6	0.875
#2	0.75	10.0	1.45	8	20.0	0.925
#3	0.75	10.0	2.45	8	20.0	0.925

In order to emphasize that the results are not solely determined by cladding tube thickness, as it is the case in the ARROW model, we recall that in the context of the single-tube approximation, the spectral distribution of the modes within the glass depends on two key parameters: the refractive index n_d of the dielectric, and the tube aspect ratio coefficient $\rho = r_{int}/r_{ext} = 1 - t/r_{ext}$ (Kharadly and Lewis, 1969; Vincetti and Setti, 2010). In this context, the slope of the μ-F curves increases with ρ and decreases with n_d (Debord et al., 2019). As a result, we anticipate a decrease in CL with higher ρ values and lower n_d values. This relationship is depicted in Figs. 3 and 4, which show the same dataset as in Fig. 2. However, these figures focus on two different TLFs with distinct physical and geometrical parameters, while having identical tube thickness as shown in Table 1. In Fig. 3, the simulated fiber is labeled as Fiber #2, differing from Fiber #1 only by a larger tube radius and consequently a larger ρ value. Despite both fibers having the same tube thickness, the results reveal significant differences in the spectral structures Fiber #2 exhibits narrower high loss region (HLR) bandwidths. This can be attributed to the steeper slope of the μ-F curves. Fiber#3, which shares the same geometrical parameters as Fiber#2 but has a higher glass index, demonstrates the impact of higher refractive index in Fig. 4. The CLMs exhibit $\mu - F$ curves with slower slopes and more spread between the $HE_{\mu,\nu}$ and $EH_{\mu,\nu}$ modes, leading to wider HLRs as shown in Fig. 4(b). Consequently, this results in higher CL and narrower TB.

3. Local azimuthal Fourier decomposition

In the previous section, we used numerical simulations to discuss the influence of CLMs azimuthal and radial indices on CL values and spectral characteristics. However, relying solely on numerical methods restricts our ability to gain deeper physical insights and predictive capabilities. To address this limitation, we introduce a mathematical approach in this section, allowing for a more effective analysis of the coupling between CLMs and CMs, and subsequently, the dynamics of CL. This approach utilizes a local azimuthal Fourier decomposition (AFD) of CMs and CLMs.
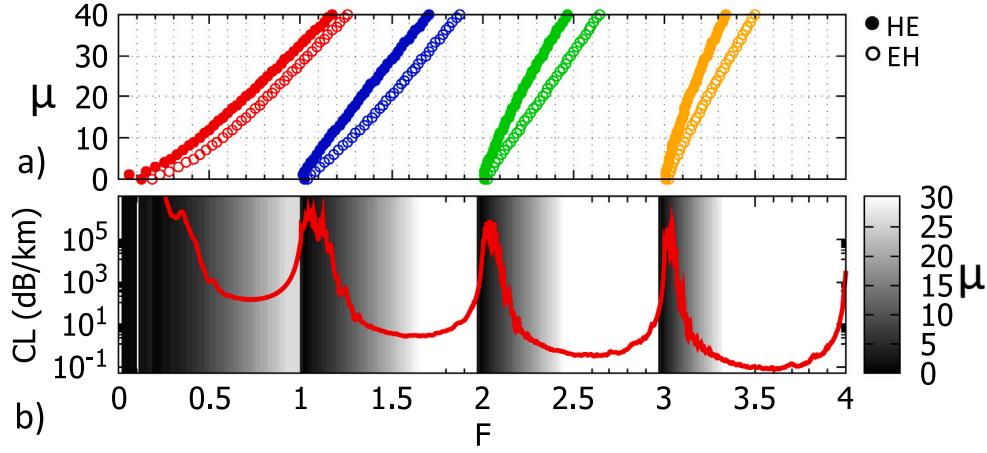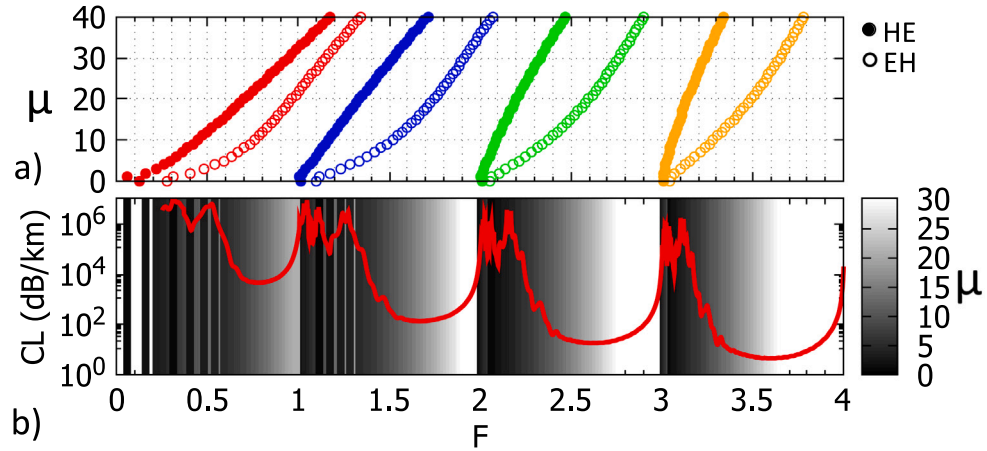
Fig. 3. Fiber #2. (a): cut-off frequencies F_c of CLMs HE (filled circles) and EH (empty circles) by varying the azimuthal index μ and for four values of the radial index ν ($\nu = 1$ red; $\nu = 2$ blue; $\nu = 3$ green; $\nu = 4$ orange). (b): CL of the LP_{01} FM. Background color related to the azimuthal index of the CLM having cut-off frequency F. (For interpretation of the references to color in this figure legend, the reader is referred to the web version of this article.)

Fig. 4. Fiber #3. (a): cut-off frequencies F_c of CLMs HE (filled circles) and EH (empty circles) by varying the azimuthal index μ and for four values of the radial index ν ($\nu = 1$ red; $\nu = 2$ blue; $\nu = 3$ green; $\nu = 4$ orange). (b): CL of the LP_{01} FM. Background color related to the azimuthal index of the CLM having cut-off frequency F. (For interpretation of the references to color in this figure legend, the reader is referred to the web version of this article.)

In the context of the single isolated tube approximation, we consider a single tube with a local frame of reference (r, θ) having the origin at the center of the tube (Vincetti and Setti, 2012), as shown in Fig. 5. Each component (radial, azimuthal, and longitudinal) of the CLM and CM electric fields is a periodic function of θ and thus can be written in terms of an azimuthal Fourier series (Baddour, 2009):

$$E_{co_s}(r, \theta) = \sum_{m_{co}=-\infty}^{+\infty} R_m^{co_s}(r) e^{jm_{co}\theta} \tag{3}$$

$$E_{cl_s}(r, \theta) = \sum_{m_{cl}=-\infty}^{+\infty} R_m^{cl_s}(r) e^{jm_{cl}\theta} \tag{4}$$

where $s = r, \theta, z$, m is the azimuthal Fourier index, and

$$R_m^{(co/cl)_s}(r) = \frac{1}{2\pi} \int_0^{2\pi} E_{(co/cl)_s}(r, \theta) e^{-jm_{co/cl}\theta} d\theta. \tag{5}$$

Fig. 6 shows an example of such an AFD for the case of tube 1 of Fiber #1 (see Fig. 5). The left hand side of the figure shows the radial and azimuthal components of the y-polarized FCM field distribution along the tube perimeter at $F = 2.6$. The orange curves are computed at the inner ($r = r_{int}$) and the red curves at the outer ($r = r_{ext}$) boundaries of the tube. The right hand side of the figure shows the AFD Spectra of this field radial components (top) and azimuthal components (bottom), which hereinafter are simply called "azimuthal spectra". The

magnitude of each component of the azimuthal spectrum is given by $R_{m_{co}}^{co_r}(r)$ for the radial field component, and by $R_{m_{co}}^{co_\theta}(r)$ for the azimuthal component. The spectra exhibit a "low pass" characteristic, in that the significant coefficients are primarily observed for azimuthal indices $|m_{co}| \leq 10$. When $m_{co} = 0$, the radial component has its maximum, whereas the azimuthal one has a zero because of the odd symmetry. Notably, similar results are obtained for the x-polarization component by interchanging the roles of the azimuthal and radial components.

To confirm the "low pass" filter property across the entire spectrum, we computed the azimuthal spectra at various normalized frequencies. Fig. 7 shows the evolution of the FCM azimuthal spectrum for varying normalized frequency within the 3rd order TB. The side of the figure shows the CL at this TB (blue curve). We can identify two significant features in these spectra. Firstly, the azimuthal spectra exhibit a "low pass" filter characteristic for the majority of the transmission band (TB) bandwidth, except for the red-edge region. In this region, the azimuthal spectrum bandwidth expands, indicating a stronger coupling between the CMs and CLMs, in consistency with our numerical results. Secondly, we note that the magnitude of the spectra calculated on the inner boundary remains relatively constant across the TB bandwidth. Conversely, for the spectra calculated on the outer boundary, they have a similar magnitude to the inner boundary spectra near the TB edges. However, as the frequency approaches the center of the TB, the magnitude decreases significantly by almost two orders of magnitude. Lastly,
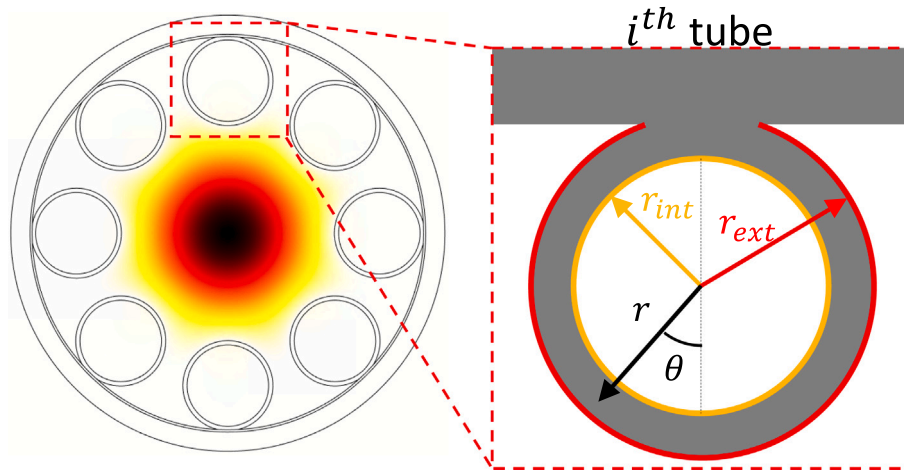
Fig. 5. Fiber cross section with FCM field distribution and detail of local polar frame of reference (r, θ) centered at the center of the *i*th tube. Red and orange curves highlight the outer and inner tube boundaries, respectively. (For interpretation of the references to color in this figure legend, the reader is referred to the web version of this article.)
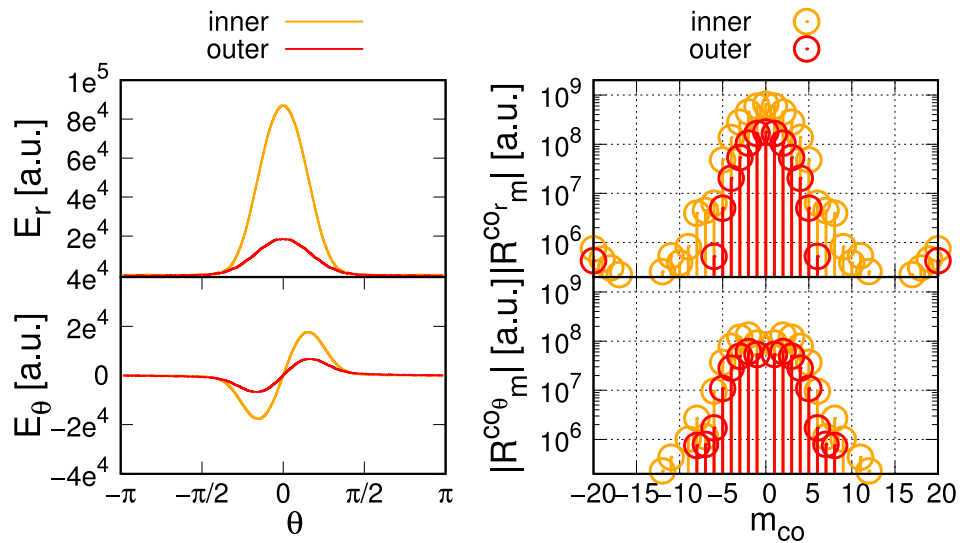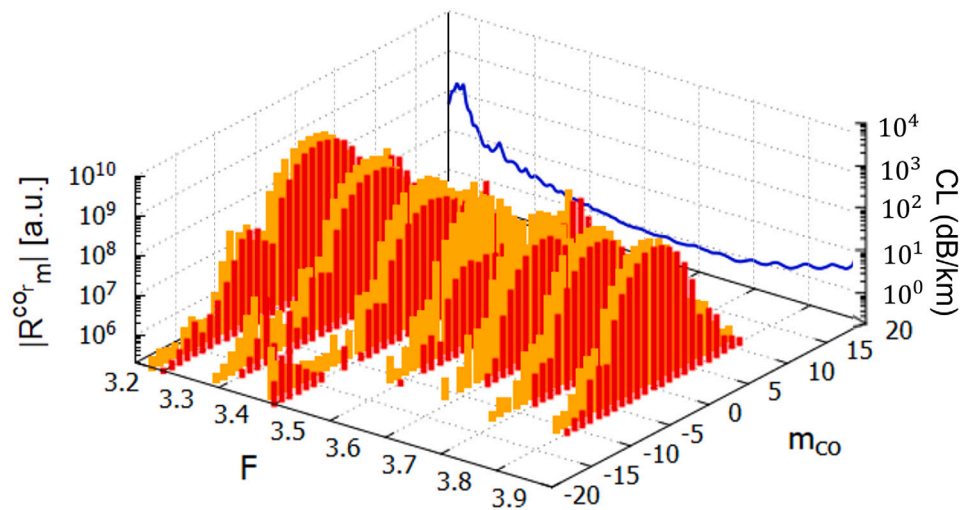

Fig. 6. Fundamental core mode. Left: radial E_{co_r} (top) and azimuthal E_{co_θ} (bottom) electric field components along the inner (orange) and outer (red) tube boundaries. Right: magnitude of the corresponding azimuthal spectra. (For interpretation of the references to color in this figure legend, the reader is referred to the web version of this article.)

Fig. 7. Azimuthal spectra of the FCM radial component E_{co_r} for different normalized frequencies, calculated along the inner (orange) and outer (red) boundaries. The CL spectrum on the same normalized frequency range is also shown. (For interpretation of the references to color in this figure legend, the reader is referred to the web version of this article.)
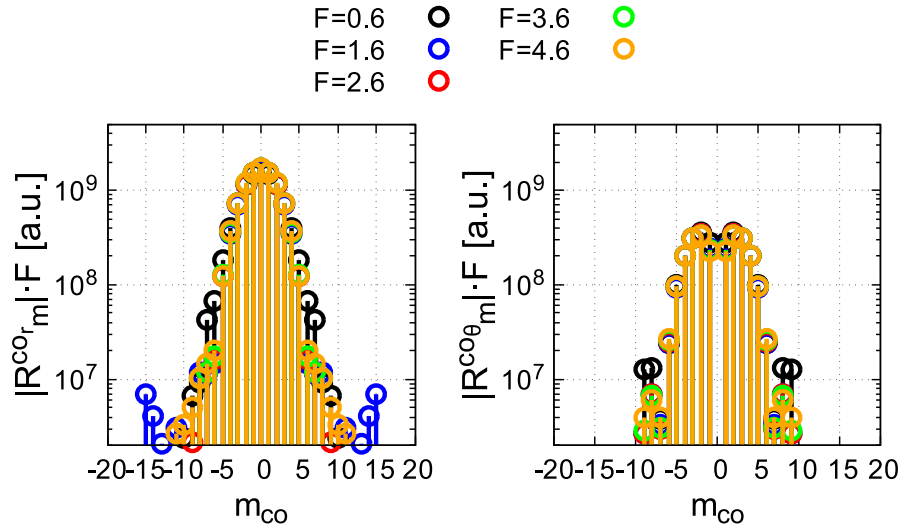
Fig. 8. FM azimuthal spectrum of the radial (left) and azimuthal (right) components at the inner boundary multiplied by the corresponding normalized frequency they are calculated at: $F = 0.6$ (black); $F = 0.6$ (blue); $F = 1.6$ (red); $F = 2.6$ (green); $F = 3.6$ (orange). (For interpretation of the references to color in this figure legend, the reader is referred to the web version of this article.)

we observed that these features hold true for all the transmission bands (TBs), except for a consistent scaling law of $1/F$. This is illustrated in Fig. 8, which compares the values of $R_m^{co_r} \cdot F$ for specific normalized frequencies, including $F = 0.6, 1.6, 2.6, 3.6, 4.6$. Remarkably, the spectra exhibit substantial overlap, confirming the validity of the relationship $R_m^{co_r} \propto 1/F$. Moreover, this scaling trend is consistent across the various components, aligning with the scaling law based on the square of the electric field at the boundaries, as previously established in the literature (Vincetti, 2016).

Figs. 9 and 10 provide insights into the characteristics of two CLMs, specifically $EH_{5,3}$ and $EH_{10,3}$. On the left-hand side, we observe the azimuthal and radial profiles of these CLMs at the inner (yellow curves) and outer (red curves) boundaries of an isolated tube. Meanwhile, the right-hand side illustrates their corresponding azimuthal spectra. Due to the sinusoidal dependence on the azimuthal angle (Kharadly and Lewis, 1969; Vincetti and Setti, 2010; Debord et al., 2017), each component of the field exhibits a double component at $|m_{cl}| = \mu$ with equal magnitudes. This symmetry arises from the fact that the imaginary parts of E_r and E_θ are significantly lower than the real parts, resulting in $R_m^{cl_s} \simeq (R_{-m}^{cl_s})^*$. It is worth noting that the spectra of the HE CLMs exhibit similar characteristics, and the same observations can be applied to them. Based on this analysis, the CLMs AFD can be written as:

$$E_{cl_s}(r, \theta) \simeq (A_p^s)^* e^{j\mu\theta} + A_p^s e^{-j\mu\theta} \tag{5}$$

with $p = HE, EH$, $s = r, \theta$, and $r = r_{int}, r_{ext}$ and thus

$$R_m^{cl_s} = \begin{cases} A_p^s & m = \mu \\ (A_p^s)^* & m = -\mu \\ 0 & |m| \neq \mu \end{cases} \tag{6}$$

4. The model

Now that we have expressed the fiber mode fields as a linear combination of azimuthal harmonics, we can utilize the AFD to explore mode coupling and its effects on confinement loss in tubular fibers. The AFD provides an effective and useful tool for calculating and obtaining semi-analytical expressions for the integrals in Eq. (2), as shown below. The integral of one of the N terms in (2) is:

$$\iint_{S_{tube}} \overline{E}_{t_{co}} \cdot \overline{E}_{t_{cl}} \, dS = \int_0^\infty \int_0^{2\pi} \left(E_{co_r} E_{cl_r} + E_{co_\theta} E_{cl_\theta} \right) r \, dr \, d\theta \tag{7}$$

By substituting (3) and (4) in (7), and recalling that:

$$\int_0^{2\pi} e^{-jn\theta} e^{-jm\theta} d\theta = \begin{cases} 0 & \text{if } m \neq -n \\ 2\pi & \text{if } m = -n \end{cases}$$

we obtain:

$$\iint_{S_{tube}} \overline{E}_{t_{co}} \cdot \overline{E}_{t_{cl}} \, dS = 2\pi \int_0^\infty g(r) dr. \tag{8}$$

where

$$g(r) = g^r(r) + g^\theta(r), \tag{9}$$

with

$$g^r(r) = \sum_{m=-\infty}^{+\infty} R_m^{co_r}(r) R_{-m}^{cl_r}(r) \tag{10}$$

$$g^\theta(r) = \sum_{m=-\infty}^{+\infty} R_m^{co_\theta}(r) R_{-m}^{cl_\theta}(r), \tag{11}$$

defined as the Azimuthal Spectra Overlap (ASO). The above can be further simplified by recalling that the CLMs are strongly localized within and around the dielectric wall of the tube, and the radial profile is solely dependent on radial index ν. Secondly the amplitudes of the FM spectral coefficients are much larger on the inner boundary than on the outer one. Consequently g can be estimated just by calculating its value on the tube inner boundary ($r = r_{int}$). Finally, the radial and azimuthal ASO, g^r and g^θ, respectively, are non-zero only if the two spectra of the corresponding components are at least partially overlapping. Thus on the basis of above and of Eq. (6), it follows:

$$g^r(r) = R_\mu^{co_r}(r_{int}) \left(A_p^r(r_{int}) \right)^* + R_{-\mu}^{co_r}(r_{int}) A_p^r(r_{int}) \tag{12}$$

$$g^\theta(r) = R_\mu^{co_\theta}(r_{int}) \left(A_p^\theta(r_{int}) \right)^* + R_{-\mu}^{co_\theta}(r_{int}) A_p^\theta(r_{int}). \tag{13}$$

According to CMT, the loss due to coupling between a core and a cladding leaky mode at the phase matching condition, $\Delta\alpha$ is proportional to $|K|^2$, and K can be estimated by $g(r_{int})$ thus for each CLM:

$$\Delta\alpha \propto |K|^2 \propto |g(r_{int})|^2. \tag{14}$$

occurring at $F = F_c$ of the involved CLM. Eqs. (12), (13) and (14), highlight as loss contribution of the coupling between FM and a CLM is primarily driven by the azimuthal spectral component of the former at the azimuthal index of the latter. It is thus the azimuthal spectral
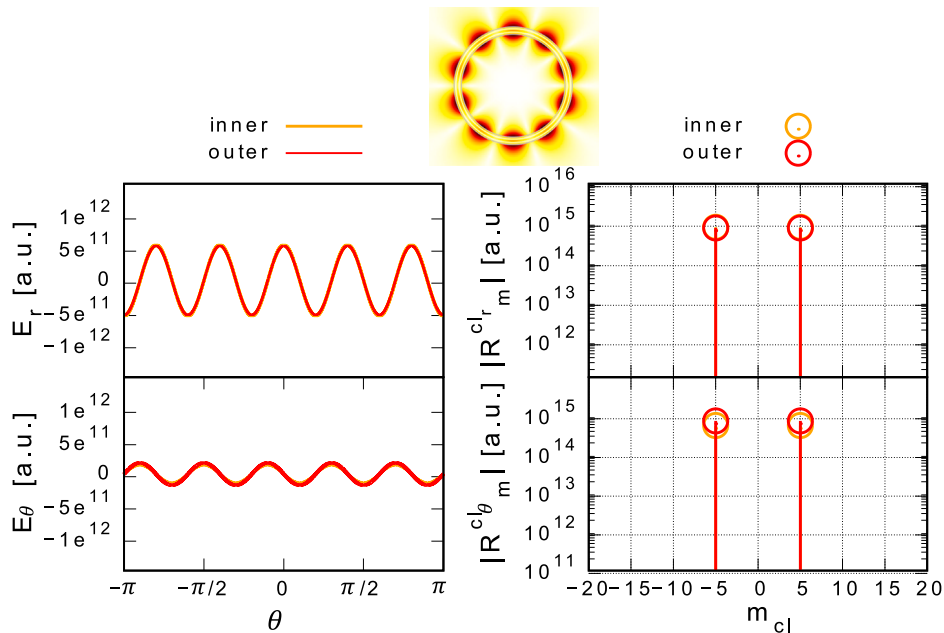
Fig. 9. Cladding mode $EH_{5,3}$. Top: Transverse electric field distribution. Left: E_{cl_r} (top) and E_{cl_θ} (bottom) profiles along the inner (orange) and outer (red) tube boundaries. Right: magnitude of the corresponding AFS. (For interpretation of the references to color in this figure legend, the reader is referred to the web version of this article.)
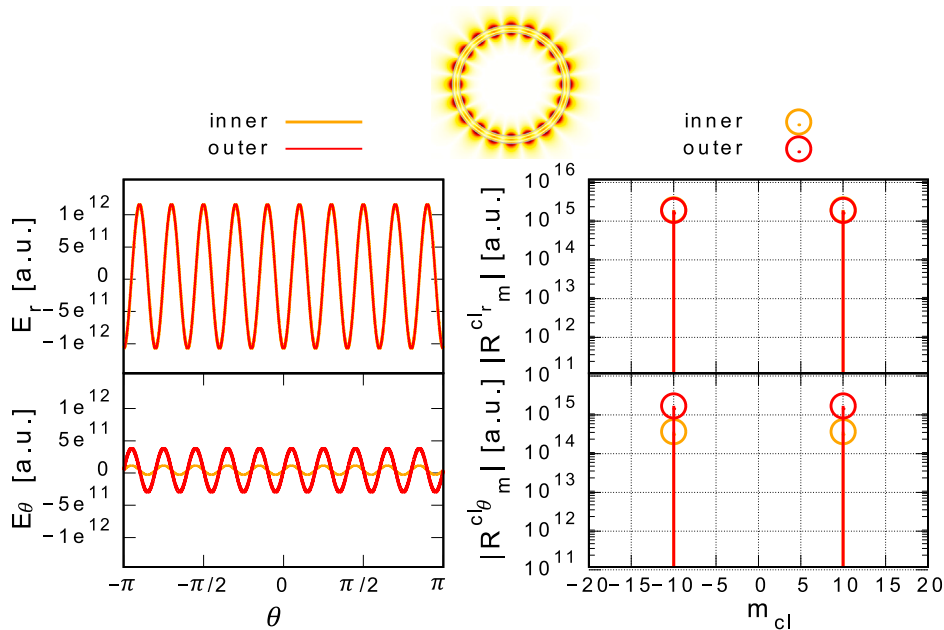

Fig. 10. Cladding mode $EH_{10,3}$. Top: Transverse electric field distribution. Left: E_{cl_r} (top) and E_{cl_θ} (bottom) profiles along the inner (orange) and outer (red) tube boundaries. Right: magnitude of the corresponding AFS. (For interpretation of the references to color in this figure legend, the reader is referred to the web version of this article.)

shape of FM which shapes the HLRs and the spectral distribution of the CLMs F_c which defines the HLR bandwidths. These statements are confirmed by the results presented and discussed in the next section.

5. Results

Fig. 11 compares the numerical results on the y-polarized FM CL of Fiber#1 with $|g|^2$ values represented by vertical bars placed at the corresponding F_c by calculating g^r and g^θ through Eqs. (12) and (13) only on tubes 1 and 3 of Fig. 1. Blue bars refer to HE CLMs and the red to EH ones. Fig. 12 shows a detail around the HLR corresponding to CLM with $\nu = 2$. Despite this and the previous described approximations, the agreement in describing the HLRs' edges is very good. The

approach also allows to quantify the individual contributions of HE and EH CLMs in defining the total CL in HLRs. Since for equal azimuthal and radial indices, F_c for the HE modes is smaller than for the EH modes (see Fig. 2(Top) and related comments), HE CLMs, and in particular those with low azimuthal index, define the red-edge of the HLRs or, in other words, the blue-edge of the TBs. For the same reason, the HLR blue-edges (or the TB red-edges) are mainly defined by the EH CLMs. In accordance with Eq. (14) comments and the ASO concept, the HLR blue-edges are mainly defined by the FM azimuthal spectrum and by the spectral distribution of the EH CLMs cut-off frequencies. The former defines the relative amplitudes of the CLMs spectral coefficients, the latter their spectral positioning. The cut-off frequencies of $EH_{\mu,\nu}$ define the transition between HLR and TB between $F = \nu - 1$ and $F = \nu$.
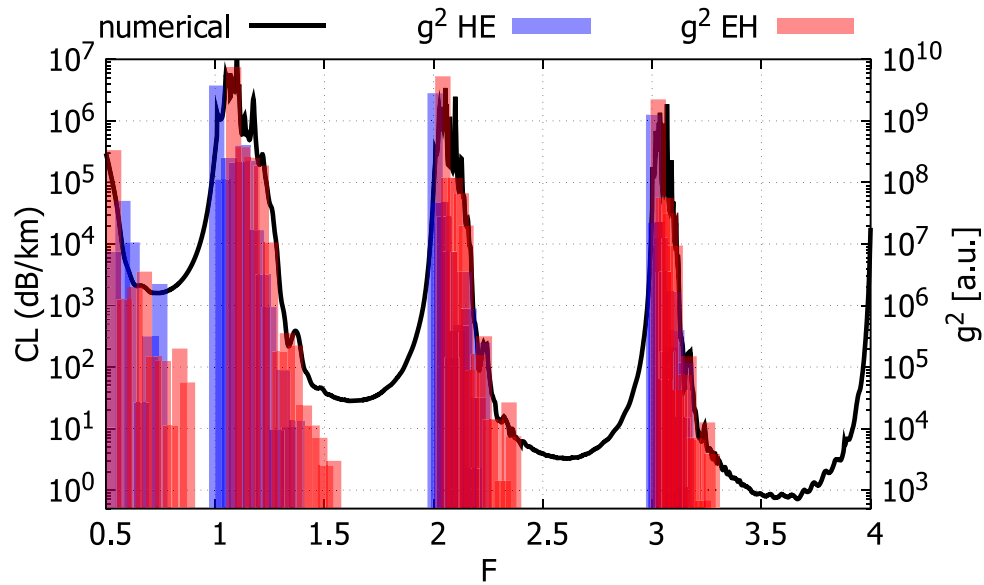
Fig. 11. Comparison of CL spectra of Fiber#1 obtained by numerical simulation (black) and $|g|^2$ computed on the inner boundaries of tubes 1 and 3 of Fig. 1. Blue and red bars refer to HE and EH CLMs respectively and are placed at the corresponding F_c. (For interpretation of the references to color in this figure legend, the reader is referred to the web version of this article.)
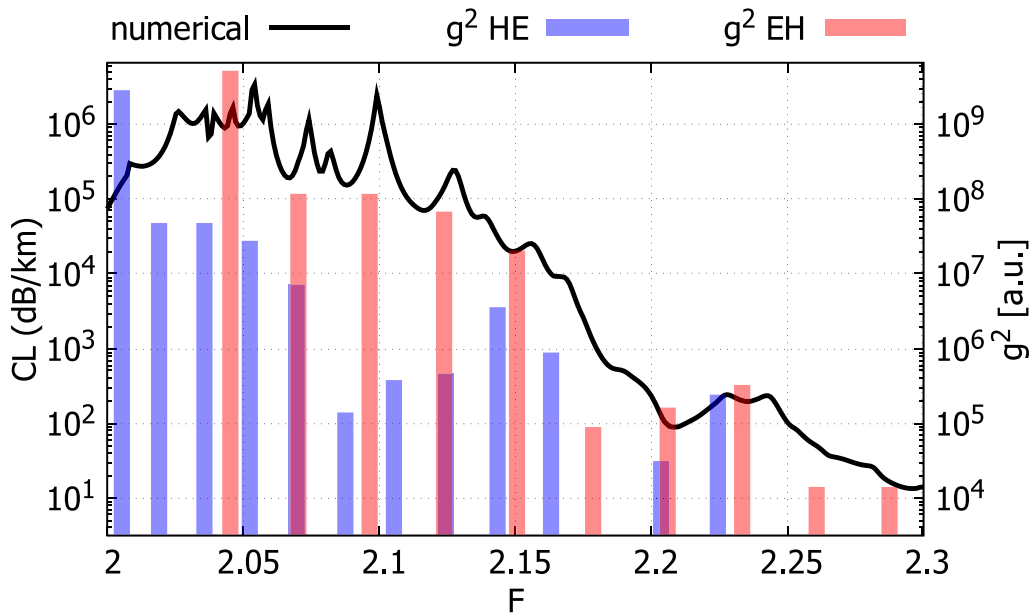

Fig. 12. Detail of the CL and $|g|^2$ comparison shown in Fig. 11 around HLR centers at $F = 2$.

As shown in Figs. 2, 3 and 4, those frequencies depend on the radial index v, the tube aspect ratio ρ, and refractive index n_d. This statement is confirmed by analyzing the numerical CL and Eq. (14) spectra of the other two TLFs reported in Table 1, as shown in Figs. 13 and 14. The model reproduces with nice accuracy the variations of the spectral bandwidths of both HLRs and TBs due to the variation of the tube aspect ratio ρ (Fig. 13 versus Fig. 11) and due to the refractive index n_d variation (Fig. 14 versus Fig. 13).

6. Conclusion

In this work, a method of analysis based on the Azimuthal Fourier Decomposition of the fiber's modes along the tube boundaries combined with Coupled Mode Theory has been developed in the framework of the inhibited-coupling model, and then applied to the loss analysis of ideal TLFs. The results show a good ability of the method to predict TLF loss irrespective of geometrical and physical fiber parameters. The method allows to highlight the crucial role played by the CMs-CLMs coupling in defining the TLF loss. In particular the spectral distribution of the CLM cut-off frequencies F_c, combined with the azimuthal spectrum of CMs electric field along the cladding tube boundaries define the main features of the HLRs and the TB bandwidth. The method has been here applied to analyze the FM CL, but it can be straightforwardly applied to higher-order CMs. Finally, the method is a useful and effective theoretical tool for analyzing the impact of fiber non-idealities on loss increase in real TLFs. The application of the approach for analyzing the impact of non-constant thickness along the tubes' perimeter is presented and discussed in Part II.
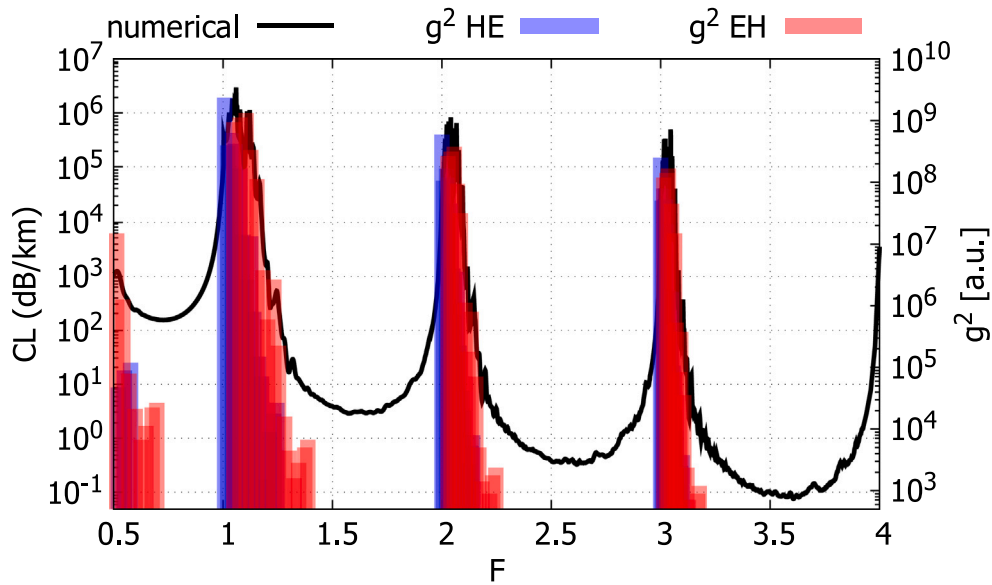
Fig. 13. Comparison of CL spectra of Fiber#2 obtained by numerical simulation (black) and $|g|^2$ computed on the inner boundaries of tubes 1 and 3 of Fig. 1. Blue and red bars refer to HE and EH CLMs respectively and are placed at the corresponding F_c. (For interpretation of the references to color in this figure legend, the reader is referred to the web version of this article.)
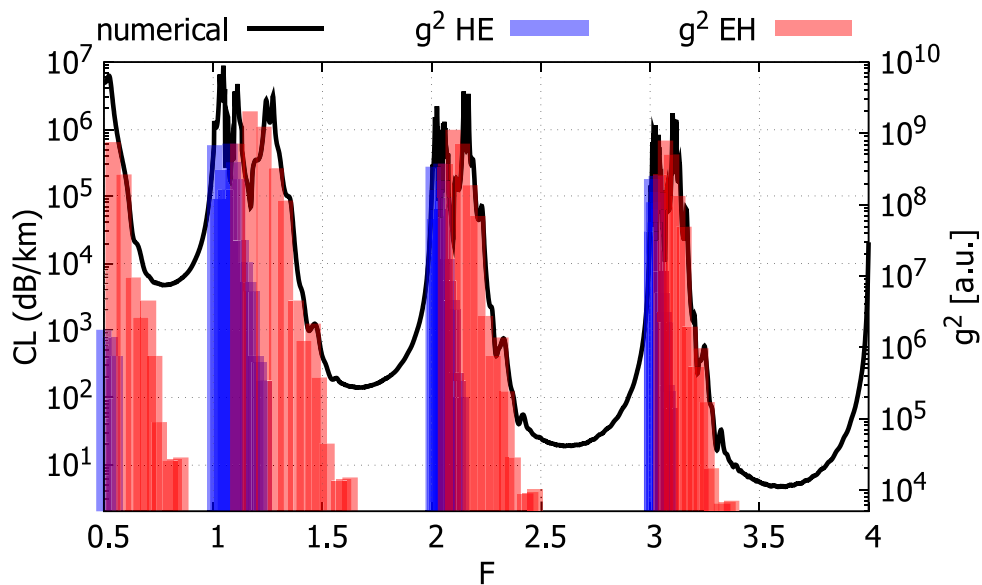

Fig. 14. Comparison of CL spectra of Fiber#3 obtained by numerical simulation (black) and $|g|^2$ computed on the inner boundaries of tubes 1 and 3 of Fig. 1. Blue and red bars refer to HE and EH CLMs respectively and are placed at the corresponding F_c. (For interpretation of the references to color in this figure legend, the reader is referred to the web version of this article.)

CRediT authorship contribution statement

Federico Melli: Investigation, Writing – original draft, Writing – review & editing, Data curation, Formal analysis, Validation. **Kostiantyn Vasko:** Investigation, Validation. **Lorenzo Rosa:** Validation, Writing – original draft, Writing – review & editing. **Fetah Benabid:** Methodology, Supervision, Writing – original draft, Writing – review & editing. **Luca Vincetti:** Conceptualization, Formal analysis, Methodology, Supervision, Writing – original draft, Writing – review & editing.

Declaration of competing interest

The authors declare the following financial interests/personal relationships which may be considered as potential competing interests: Federico Melli reports financial support was provided by European

Data availability

Data will be made available on request.

Acknowledgments

References

Amrani, F., Osório, J.H., Delahaye, F., Giovanardi, F., Vincetti, L., Debord, B., Gérôme, F., Benabid, F., 2021. Low-loss single-mode hybrid-lattice hollow-core photonic-crystal fibre. Light Sci. Appl. 10 (1), 7.

Baddour, N., 2009. Operational and convolution properties of two-dimensional Fourier transforms in polar coordinates. J. Opt. Soc. Amer. A 26 (8), 1767–1777.

Belardi, W., Knight, J.C., 2014. Hollow antiresonant fibers with reduced attenuation. Opt. Lett. 39 (7), 1853–1856.

Bomse, D.S., Ediger, M.N., 2014. Simultaneous detection of multiple gases by Raman spectroscopy with hollow-core fibers. In: 2014 Conference on Lasers and Electro-Optics (CLEO) - Laser Science To Photonic Applications.

Chen, X., Ding, W., Wang, Y.-Y., Gao, S.-F., Xu, F., Xu, H., Hong, Y.-F., Sun, Y.-Z., Wang, P., Lu, Y.-Q., Zhang, L., 2021. High-fidelity, low-latency polarization quantum state transmissions over a hollow-core conjoined-tube fiber at around 800nm. Photon. Res. 9 (4), 460–470.

Couny, F., Benabid, F., Roberts, P.J., Light, P.S., Raymer, M.G., 2007. Generation and photonic guidance of multi-octave optical-frequency combs, 318 (5853), 1118–1121 http://dx.doi.org/10.1126/science.1149091.

Cregan, R.F., Mangan, B.J., Knight, J.C., Birks, T.A., Russell, P.S.J., Roberts, P.J., Allan, D.C., 1999. Single-mode photonic band gap guidance of light in air 285 (5433), 1537–1539 http://dx.doi.org/10.1126/science.285.5433.1537.

Debord, B., Alharbi, M., Bradley, T., Fourcade-Dutin, C., Wang, Y., Vincetti, L., Gérôme, F., Benabid, F., 2013a. Hypocycloid-shaped hollow-core photonic crystal fiber part I: Arc curvature effect on confinement loss. Opt. Express 21 (23), 28597–28608.

Debord, B., Amrani, F., Vincetti, L., Gérôme, F., Benabid, F., 2019. Hollow-core fiber technology: The rising of "Gas Photonics". Fibers 7 (2).

Debord, B., Amsanpally, A., Alharbi, M., Vincetti, L., Blondy, J., Gérôme, F., Benabid, F., 2015. Ultra-large core size hypocycloid-shape inhibited coupling kagome fibers for high-energy laser beam handling. J. Lightwave Technol. 33 (17), 3630–3634. http://dx.doi.org/10.1109/JLT.2015.2448794.

Debord, B., Amsanpally, A., Chafer, M., Baz, A., Maurel, M., Blondy, J.M., Hugonnot, E., Scol, F., Vincetti, L., Gérôme, F., Benabid, F., 2017. Ultralow transmission loss in inhibited-coupling guiding hollow fibers. Optica 4 (2), 209–217.

Debord, B., Jamier, R., Gérôme, F., Leroy, O., Boisse-Laporte, C., Leprince, P., Alves, L.L., Benabid, F., 2013b. Generation and confinement of microwave gas-plasma in photonic dielectric microstructure. Opt. Express 21 (21), 25509–25516.

Ding, W., Wang, Y.-Y., Gao, S.-F., Wang, M.-L., Wang, P., 2020. Recent progress in low-loss hollow-core anti-resonant fibers and their applications. IEEE J. Sel. Top. Quantum Electron. 26 (4), 1–12. http://dx.doi.org/10.1109/JSTQE.2019.2957445.

Duguay, M., Kokubun, Y., Koch, T.L., Pfeiffer, L., 1986. Antiresonant reflecting optical waveguides in SiO2-Si multilayer structures. Appl. Phys. Lett. 49 (1), 13–15.

Gao, S.-F., Wang, Y.-Y., Ding, W., Hong, Y.-F., Wang, P., 2019. Hollow-core conjoined-tube negative-curvature fiber with loss approaching Rayleigh scattering limit of silica. In: Conference on Lasers and Electro-Optics. Optical Society of America, p. STh1L.6.

Hoang, V.T., Kasztelanic, R., Stepniewski, G., Xuan, K.D., Long, V.C., Trippenbach, M., Klimczak, M., Buczynski, R., Pniewski, J., 2020. Femtosecond supercontinuum generation around 1560 nm in hollow-core photonic crystal fibers filled with carbon tetrachloride. Appl. Opt. 59 (12), 3720–3725.

Hong, Y., Bradley, T.D., Taengnoi, N., Bottrill, K.R.H., Hayes, J.R., Jasion, G.T., Poletti, F., Petropoulos, P., Richardson, D.J., 2021. Hollow-core NANF for high-speed short-reach transmission in the S+C+L-bands. J. Lightwave Technol. 39 (19), 6167–6174. http://dx.doi.org/10.1109/JLT.2021.3097278.

Hsu, C., Zhen, B., Stone, A.D., Joannopoulos, J.D., 2016. Bound states in the continuum. Nat. Rev. Mat. 1 (9), 16048.

Jasion, G., Sakr, H., Hayes, J., Sandoghchi, S., Hooper, L., Numkam Fokoua, E., Saljoghei, A., Mulvad, H., Alonso, M., Taranta, A., Bradley, T., Davidson, I.A., Chen, Y., Richardson, D., Poletti, F., 2022. 0.174 dB/km hollow core double nested antiresonant nodeless fiber (DNANF). In: 2022 Optical Fiber Communications Conference and Exhibition. OFC, pp. 1–3.

Jaworski, P., Krzempek, K., Dudzik, G., Sazio, P.J., Belardi, W., 2020. Nitrous oxide detection at 5.26 μm with a compound glass antiresonant hollow-core optical fiber. Opt. Lett. 45 (6), 1326–1329.

Kharadly, M., Lewis, J., 1969. Properties of dielectric-tube waveguides. Proc. Inst. Electr. Eng. 116, 214–224, (10).

Khozeymeh, F., Melli, F., Capodaglio, S., Corradini, R., Benabid, F., Vincetti, L., Cucinotta, A., 2022. Hollow-core fiber-based biosensor: A platform for lab-in-fiber optical biosensors for DNA detection. Sensors 22 (14).

Kogelnik, H., 1988. Theory of optical waveguides. In: Tamir, T. (Ed.), Guided-Wave Optoelectronics. Springer Berlin Heidelberg, Berlin, Heidelberg, pp. 7–88.

Melli, F., Giovanardi, F., Vasko, K., Rosa, L., Benabid, F., Vincetti, L., 2022. Azimuthal Fourier decomposition for loss analysis of hollow-core tube lattice fibers part II: Tube thickness variation effects. J. Lightwave Technol..

Nampoothiri, A.V.V., Jones, A.M., Fourcade-Dutin, C., Mao, C., Dadashzadeh, N., Baumgart, B., Wang, Y., Alharbi, M., Bradley, T., Campbell, N., Benabid, F., Washburn, B.R., Corwin, K.L., Rudolph, W., 2012. Hollow-core optical fiber gas lasers (HOFGLAS): a review. Opt. Mater. Express 2 (7), 948–961.

Osório, J., Amrani, F., Delahaye, F., Dhaybi, A., Vasko, K., Melli, F., Giovanardi, F., Vandembroucq, D., Tessier, G., Vincetti, L., Debord, B., Gérôme, F., Benabid, F., 2023. Hollow-core fibers with reduced surface roughness and ultralow loss in the short-wavelength range. Nat. Comm. 14 (1), 1146.

Pryamikov, A.D., Biriukov, A.S., Kosolapov, A.F., Plotnichenko, V.G., Semjonov, S.L., Dianov, E.M., 2011. Demonstration of a waveguide regime for a silica hollow-core microstructured optical fiber with a negative curvature of the core boundary in the spectral region > 3.5 μm. Opt. Express 19 (2), 1441–1448.

Roberts, P.J., Couny, F., Sabert, H., Mangan, B.J., Williams, D.P., Farr, L., Mason, M.W., Tomlinson, A., Birks, T.A., Knight, J.C., Russell, P.S., 2005. Ultimate low loss of hollow-core photonic crystal fibres. Opt. Express 13 (1), 236–244.

Sakr, H., Chen, Y., Jasion, T.G., Bradley, T., Hayes, J.R., Mulvad, H.C.H., Davidson, I.A., Fokoua, E.N., Poletti, F., 2020. Hollow core optical fibres with comparable attenuation to silica fibres between 600 and 1100 nm. Nature Commun. 11.

Setti, V., Vincetti, L., Argyros, A., 2013. Flexible tube lattice fibers for terahertz applications. Opt. Express 21 (3), 3388–3399.

Vincetti, L., 2016. Empirical formulas for calculating loss in hollow core tube lattice fibers. Opt. Express 24 (10), 10313–10325.

Vincetti, L., Rosa, L., 2019. A simple analytical model for confinement loss estimation in hollow-core tube lattice fibers. Opt. Express 27 (4), 5230–5237.

Vincetti, L., Setti, V., 2010. Waveguiding mechanism in tube lattice fibers. Opt. Express 18 (22), 23133–23146.

Vincetti, L., Setti, V., 2012. Extra loss due to Fano resonances in inhibited coupling fibers based on a lattice of tubes. Opt. Express 20 (13), 14350–14361.

Wang, Y.Y., Wheeler, N.V., Couny, F., Roberts, P.J., Benabid, F., 2011. Low loss broadband transmission in hypocycloid-core kagome hollow-core photonic crystal fiber. Opt. Lett. 36 (5), 669–671.

Weiblen, R.J., Menyuk, C.R., Gattass, R.R., Shaw, L.B., Sanghera, J.S., 2016. Fabrication tolerances in As2S3 negative-curvature antiresonant fibers. Opt. Lett. 41 (11), 2624–2627.